



Microstructure–Hardness–Corrosion Performance of 17–4 Precipitation Hardening Stainless Steels Processed by Selective Laser Melting in Comparison with Commercial Alloy

C. Garcia-Cabezon¹ · M. A. Castro-Sastre² · A. I. Fernandez-Abia² · M. L. Rodriguez-Mendez³ · F. Martin-Pedrosa¹

Received: 22 September 2021 / Accepted: 14 December 2021 / Published online: 10 April 2022
© The Author(s) 2022

Abstract

The 17–4 Precipitation Hardening Stainless Steel (PH SS) manufactured by Selective Laser Melting (SLM) has wide application perspectives, but they are limited due to defects and anisotropy. The selection of the appropriate process variables plays a fundamental part in the microstructure and in the determination of the final mechanical and corrosion properties. The main purpose of this study is to analyze the corrosion behavior, hardness and microstructure of 17–4 PH SS manufactured by SLM in comparison to the commercial counterparts. The anisotropic behavior was investigated by analyzing the microstructure–hardness and corrosion interrelationship, both in the surface of the construction platform and in the growth direction of the element. The corrosion behavior of the SLM 17–4PH SS in its natural state was investigated in relation to that of the 17–4 PH SS heat treated in a 0.1 M NaCl + 0.5 M H₂SO₄ solution, using three electrochemical techniques. The results confirmed that the corrosion resistance of SLM 17–4 PH SS was considerably better than that of the forging, even after 60 days of immersion in the test solution. This was attributed to the absence of important manufacturing defects, to the fine microstructure with an important amount of austenite produced by SLM, and to a small amount of non-metallic inclusions precipitated as a result of the fast cooling and the high speed of solidification associated with the SLM process.

Keywords Additive manufacturing · 17–4 PH SS · SLM · Microstructure · Corrosion

1 Introduction

Selective Laser Melting (SLM) is a Laser-Powder Bed Fusion (L-PBF) process that can create functional metal parts, and which provides significant advantages over conventional manufacturing processes. Yap et al. [1] reported that the SLM process is particularly advantageous for manufacturing parts with complex geometries, optimizing the strength-to-weight ratio. This property of manufacturing lightweight parts makes the SLM process especially

interesting in the aeronautics and automotive industries, where it is essential to reduce the weight of the components [2]. The work carried out by Maconachie et al. revealed the ability of the SLM process to manufacture [3] with improved mechanical and geometric properties.

SLM can process a wide variety of metals, but the most investigated have been titanium, nickel-based alloy and stainless steels. The 17–4 PH SS is a martensitic precipitation hardened stainless steel widely processed using SLM. This material has good weldability and is therefore suitable for processing by SLM [4]. The main applications of 17–4 PH SS are in the aerospace, automotive, naval, and chemical industries, where it is essential for the metal components to have a good combination of strength and corrosion resistance, such as turbine blades, piston rings, or injection molds with conformal cooling channels. These properties, which are intrinsic to the commercial 17–4 PH SS, can be modified by the SLM process.

The parts created by SLM have different properties compared to the parts manufactured by other conventional processes due to the manufacturing method. SLM uses a

✉ C. Garcia-Cabezon
crigar@eii.uva.es

¹ Materials Engineering, E.I.I., Universidad de Valladolid, Valladolid 47011, Spain

² Department of Mechanical, Informatics and Aerospace Engineering, University of León, Campus de Vegazana, León 24071, Spain

³ UVASENS, E.I.I., Universidad de Valladolid, Valladolid 47011, Spain

focused laser beam to melt and fuse the metal powder spread on the work platform. The molten material quickly solidifies forming the final part. During the melting and solidification, the material experiences thermal fluctuations with local rapid heating and cooling rates, inducing microstructure variations. This mechanism is responsible for producing parts with high residual stress, as demonstrated by Fang et al. [5]. Another characteristic of SLM manufactured parts is the porosity, which can be produced for various reasons, such as an improper setting of the processing variables or during the gas atomization process [6].

Despite the large amount of recent research, most studies on 17–4 PH SLM have focused on analyzing the influence of the process parameters on the microstructure and mechanical properties [7, 8]. They have also searched for different strategies to improve mechanical [9, 10] and fatigue behavior [11–14]. The effect of part size and geometry on melt pool dimensions and porosity, and the relationship between porosity percentage and fatigue strength, have also been investigated [8].

Corrosion resistance is an important characteristic for 17–4 PH SS SLM applications. Most studies on the corrosion properties for SLM-produced stainless steel are mainly focused on austenitic SS (AISI 316L and AISI 304) [15]; while there is a lack of knowledge concerning the behavior of SLM PH SS. Most research work on 17–4 PH stainless steel has focused on analyzing the relationship between porosity and corrosion properties. Irrinki et al. [16] have studied the effect of the powder characteristics and the energy density on the corrosion resistance of 17–4 PH SS fabricated by laser-powder bed fusion. They concluded that density is the main factor affecting the corrosion resistance in the NaCl solution. The same conclusion was reached in the study by Schaller et al. [17], where they concluded that porosity, and especially larger pores, are responsible for the worse performance and corrosion resistance [18] of the parts in comparison to forgings.

Most of the work carried out has focused on the effect of porosity on all the characteristics of steel, mechanical resistance and also corrosion resistance. There are, however, fewer studies on other factors that may also influence the work in this regard. The work by Alnajjar et al. [19], for instance, on the influence of the microstructure on the corrosion resistance of SLM 17–4 PH in acidic chloride medium concludes that the microstructure has no effect on the general corrosion behavior if the chemical composition matches. They give a much more important role to the content of manganese sulfide inclusions in the susceptibility to localized corrosion. In addition, a recent study by Wang and al. [20], on SLM 15–5 PH steel, has shown that the processing parameters (low laser power, high scanning speed, and laser energy) are the key to reducing manufacturing defects. It should not be ignored that the defects (micro-cracks, binding defects, and

voids) decrease the strength and plasticity of the material. Furthermore, it also results in a sharp decrease in resistance to pitting/crevice corrosion, especially when they exist at the bottom or interface of molten pool line [20]. These authors have also studied the heat treatments that can enhance the corrosion resistance and its relationship with the microstructural changes experienced by SLM 15–5 PH SS [21]. Stoudt et al. [22] also agree with the need for post-construction heat treatments to eliminate chemical segregation. Mujib et al. [23] indicate that the best corrosion resistance is provided by the MoS₂ coatings, as indicated by the OCP results. 17–4 PH steel, fabricated by additive manufacturing, will therefore have a behavior similar to that of wrought stainless steel.

In our case, we carried out a preliminary study [24] to optimize the processing parameters, which allowed us to obtain an almost complete densification and a low chemical segregation so as to perhaps be able to suppress the post-construction heat treatments. The analysis of the relationship between the structural modifications inherent to the SLM process (without post-construction treatments) and the corrosion behavior in a highly aggressive solution is the main objective of this work.

This paper provides a detailed analysis of the corrosion behavior of SLM 17–4 PH SS in build condition and the comparative study with commercial wrought heat treatment 17–4 PH SS. For this purpose, the microstructure and hardness of the SLM samples were analyzed. The corrosion tests were carried out using electrochemical techniques in a highly aggressive medium (acid with chlorides). In addition to the anodic polarization curves, usually used to study the corrosion behavior of SLM 17–4 PH SS, the electrochemical impedance technique was used. It was thus possible to evaluate the passive behavior of the samples in their original state and after 60 days of exposure to the test solution. A relationship between the microstructure and corrosion properties was established.

2 Experimental

2.1 Materials and Sample Preparation

Longitudinal and transversal specimens were taken from a 25.4 mm diameter round bar; the samples were identified as Wrought Longitudinal Direction (W-LD) and Wrought Transversal Direction (W-TD), respectively. The chemical composition of the commercial 17–4 PH SS samples is shown in Table 1. The W 17–4 PH SS was in solution annealed and double precipitation hardening condition. The solution heat treatment was performed at 1040 °C for 130 min, followed by air cooling to room temperature. The first step of the precipitation hardening is to hold the specimens at 625 °C for 7 h, followed by air cooling to room

Table 1 Chemical composition of the 17–4 PH SS powder for the SLM and for the W17–4 PH SS samples

Elements	C	Cr	Ni	Mo	Mn	Si	Cu	Nb	N	S	Al	Fe
Powder	–	16.93	4.17	–	0.58	0.62	3.56	0.21	–	–	–	Bal
Wrought	0.032	15.70	4.30	0.15	0.61	0.27	3.13	0.255	0.004	0.0005	0.005	Bal

Units in weight percent

temperature; while the second is to hold the specimens at 630 °C for 9.5 h, then air cooling to room temperature.

Commercially available gas-atomized spherical 17–4 PH SS powder, with a chemical composition (in wt%) listed in Table 1, was used in this study for the SLM samples. The

chemical composition (wt%) of wrought 17–4 PH SS is also reported in Table 1. The amount of chromium and copper were slightly higher for 17–4 PH SS powder.

The Scanning Electron Microscope (SEM) micrograph (Fig. 1a) shows a powder morphology that is almost

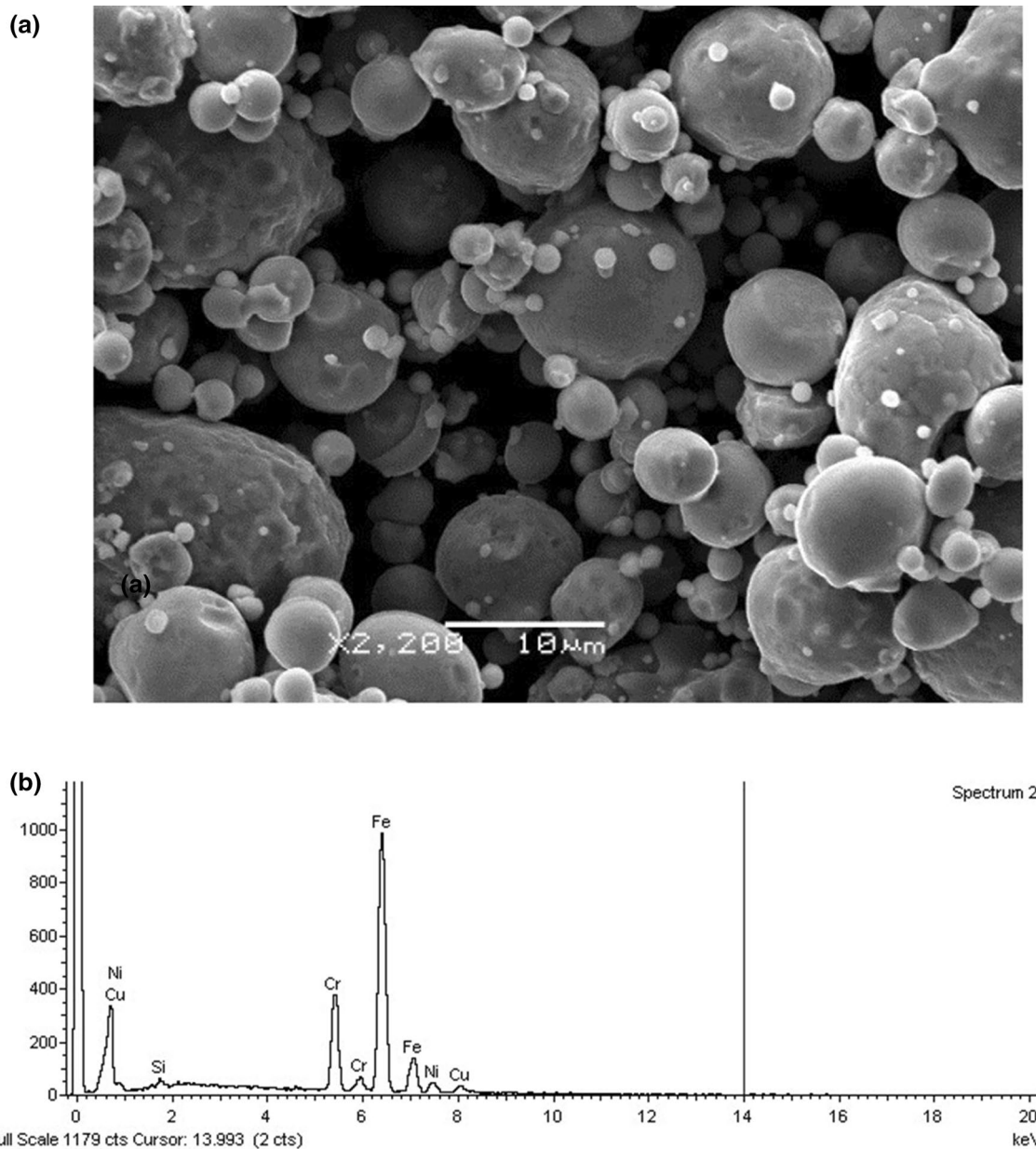
**Fig. 1** SEM micrograph of the 17–4 SS powder morphology **a** and EDS analysis of powder **b**

Table 2 Particle size distribution of the 17–4PH SS by laser diffraction

	d ₁₀	d ₅₀	d ₉₀
Particle Size (μm)	4.56	15.11	43.76

Table 3 Main processing parameters used for SLM samples

Parameter	Value
Laser power (W)	38
Scanning speed (mm/s)	140
Layer thickness (μm)	30
Hatch spacing (μm)	70
Scanning strategy	Hexagons

spherical in shape. The Energy-dispersive X-ray spectroscopy (EDX-ray) spectra of the entire area showed the existence of the elements in a greater percentage by weight in the powder (Fig. 1b).

The LS 13 320 Beckmann Coulter laser diffraction particle size analyzer had been used to determine the size distribution of the powder particles. Table 2 shows the fraction of the population below 10%, 50% and 90% of the accumulative frequency distribution using the parameters d₁₀, d₅₀ and d₉₀.

The SLM samples were cubic specimens with dimensions 12 × 12 × 8 mm, fabricated at the UFI 3D Laboratory (University of León, Spain) using a ProX 100 SLM machine (3DSystems). DMP ProX Manufacturing software was used to design the cubic specimens and to go from an STL file to a FAB3 file for direct transfer to the SLM machine. The processing parameters were set according to the manufacturer's recommendations. The hexagonal scanning strategy is recommended for 3D Systems metal printers in order to achieve high density parts and good mechanical properties. The layer height of 30 microns is the recommended value for printing 17–4 PH steel parts on the ProX 100 SLM machine. This value is set by default in the parameters of the said machine. This layer height allows high precision parts to be obtained. The main processing parameters are indicated in Table 3. The printing procedure was carried out in a protecting chamber, using nitrogen to maintain an oxygen level below 1000 ppm and thus avoid the oxidation of the powder.

The SLM samples were analyzed in two sections: first, in the x–y build plane; and second, in the x–z plane (perpendicular to the build direction) according to ASTM 52,900 [25]. The superficial and transverse directions of these samples are denoted as SLM-Superficial Direction (SLM-SD) and SLM-Transversal Direction (SLM-TD), respectively.

2.2 Microstructural Characterization

Microstructural characterization was done with optical metallography and scanning electronic microscopy with energy dispersive analysis of X-rays (SEM/EDS) using SEM-FEI (QUANTA 200F). To obtain microstructural features, a diamond suspension (1 μm) was used for polishing and different attack reagents (Vilella, Fry and oxalic acid solutions) were used for chemical and electrochemical etching. The degree of residual porosity for SLM samples was determined by image analysis (Image J). X-ray diffraction (XRD) using Agilent SuperNova was used in the identification of some of the phases. A Ferrite meter was used to measure the Ferrite number (FN) or Ferrite Percentage (% F) of stainless steel.

2.3 Vickers Hardness

Macrohardness was measured by the Vickers test with 30 kg for 30 s using a Centaur 920 Durometer. Five impressions were made on the center section of the specimen, while the mean hardness and standard deviation were also determined.

The results of the macro-hardness test can be influenced by the possible effect of the porosity of the SLM samples. Therefore, a micro-hardness test was also performed with a Matsuzawa MXT70 micro-hardness meter with a 100 g load during 30 s. The microhardness was evaluated as the arithmetic mean value of at least ten hardness tests with acceptable impressions after discarding the two lowest values.

2.4 Corrosion Resistance

Three electrochemical methods were used to characterize the corrosion resistance of Wrought and SLM samples: Open Circuit Potential (OCP), Anodic Polarization measurement (PA) and Electrochemical Impedance Spectroscopy (EIS), using a potentiostat 273A EG&G PAR and an impedance analyzer Solartron SI 1260. The corrosion tests were carried out in acid solution with chlorides (0.5 M NaCl + 0.5 M H₂SO₄ at 30 °C) in a three-electrode conventional cell using a Saturated Calomel Electrode (SCE) as the reference electrode and graphite as the counter-electrode. The test was performed in deoxygenated conditions (purged with nitrogen). The samples were wet ground with SiC abrasive papers, followed by polishing with 1 mm diamond aqueous suspension.

The open circuit potential was measured for 3600 s of immersion of the samples in the electrolyte solution. Potentiodynamic anodic potential curves were made following the ASTM G-5 [26]. Once a nearly quasi-stable potential had been reached, the anodic potentiodynamic scan started at 50 mV below V_{OCP}, reaching 1000 mV_{SCE}, using 50 mV/min as the potential scan rate. The corrosion potential and current densities were obtained through Tafel's analysis and was carried out to evaluate the corrosion polarization resistance

(R_p). Impedance spectra were performed at open circuit potential after a stabilization step at open circuit during 1800s with a signal amplitude of 10 mV at OCP and with a frequency range from 10 MHz to 0.1 Hz. Impedance results were fitted to equivalent circuits using CorrView software. To ensure statistical accuracy, the electrochemical essays were repeated three times. Observations by optical microscopy were done on the corroded samples to understand how the processing procedures influence the corrosion performance of 17–4 PH SS.

3 Results

3.1 Microstructure Characterization

The microstructure study of the 17–4 PH SLM samples in the as-built condition was carried out in two sections, i.e., SD and TD. The microstructure of the wrought samples after heat-treatment was analyzed in transversal and longitudinal sections to cold rolled direction, denoted as TD and LD, respectively.

Representative micrographs of polished SLM-SD and SLM-TD are displayed in Fig. 2a and b; both sections show a low level of porosity, the porosity percentage obtained by image analysis was 0.5% for LM-SD and 0.8% for SLM-TD, which suggests that the processing parameters were optimized. Suryawanshi et al. [27] confirmed that porosity and inclusion content are two important microstructural features related to corrosion behavior. Porosity is a typical fault in SLM parts; they can be spherical associated with gas entrapment during the solidification process or irregular due to unmelted powder particles or insufficient overlap between the scan tracks, as observed by Aboulkhair et al. [28]. Moreover, Suryawanshi et al. [29] found that the porosity level depended on such factors as the orientation of the surface in relation to the direction of construction and the scanning strategy.

The microstructure of wrought samples was pore free; the dark points observed in Fig. 2c correspond to non-metallic inclusions (oxides and manganese sulfides).

Figure 3a and b show the microstructure of W-TD and W-LD, respectively; while Fig. 3c and d show the microstructures of the SLM-SD and SLM-TD. It is clear that SLM processing produced microstructures that are different from those of conventional processes. For SLM samples, there are important differences, depending on the orientation of the surface; while similar microstructures were observed for W-TD and W-LD, which had a fully martensitic microstructure (the prior austenite ASTM grain size number G was 8.0) with small carbide precipitates but without ferrite delta stringers (0%). This is consistent with the literature for heat-treated 17–4 PH SS [30]. The melt pool shapes and

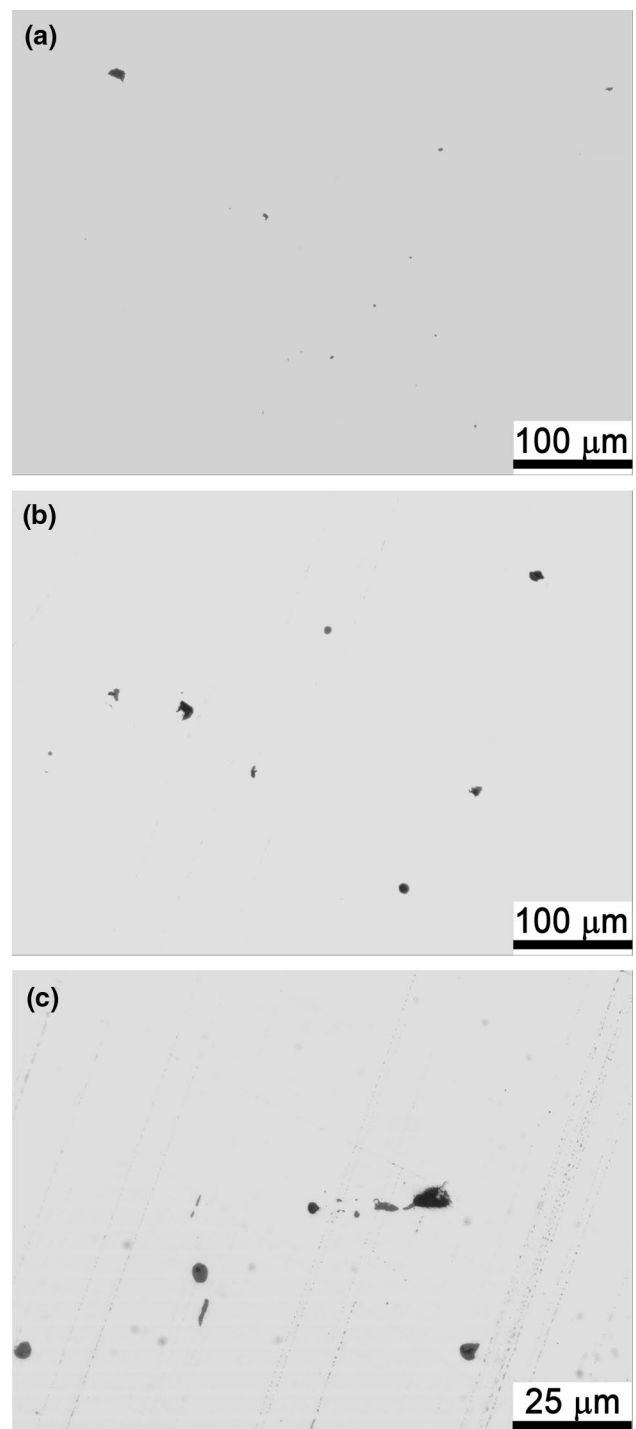


Fig. 2 Optical microstructure polishing of **a** SLM-SD, **b** and **c** SLM-TD

laser tracks are the most important microstructural features of the SLM as-built condition. Figure 3d clearly shows the overlapping hemispherical melt pools created by the laser in the normal orientation to the build direction, SLM-TD. The average diameter of the molten pool structure was

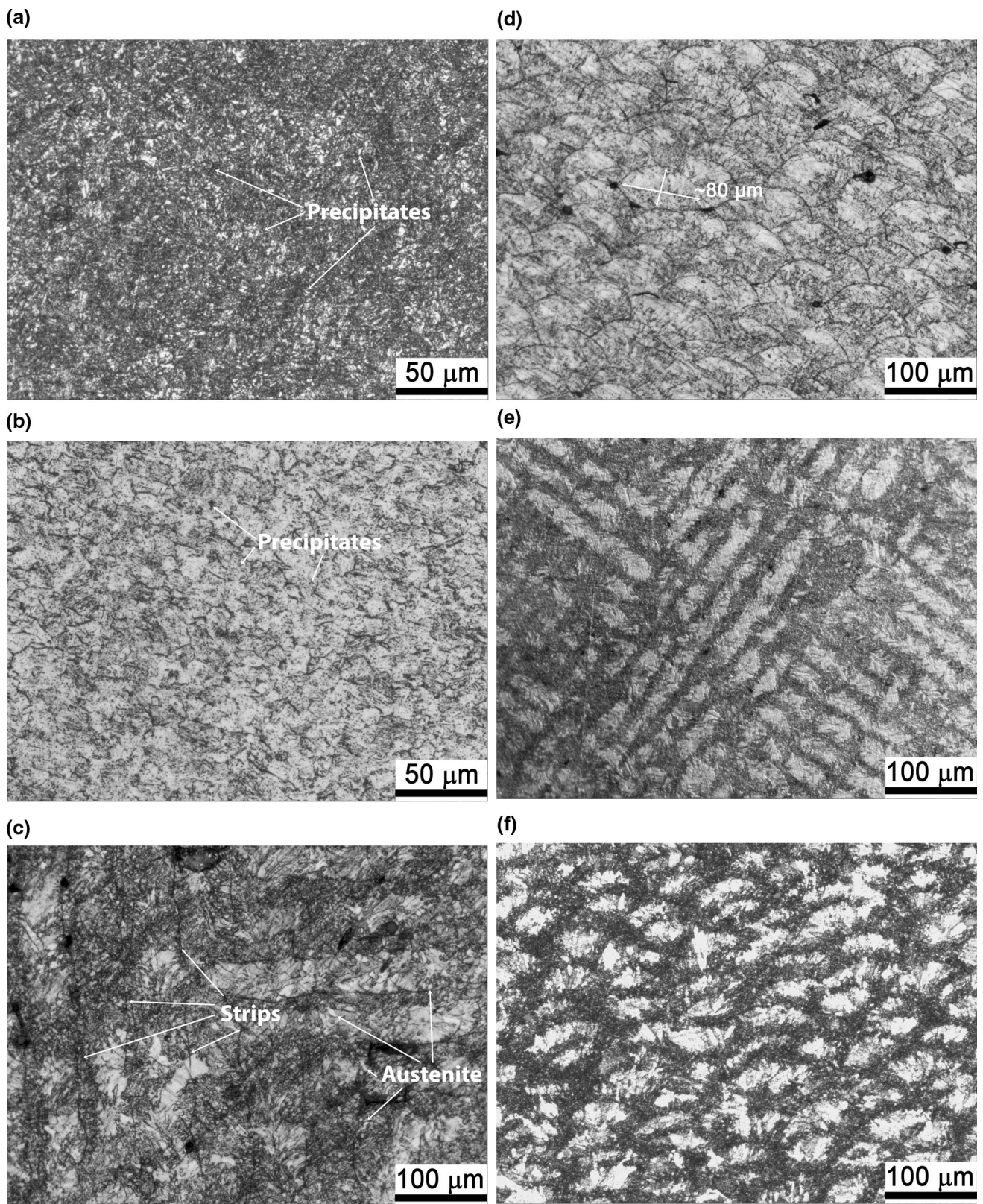


Fig. 3 Microstructure of **a** W-TD, **b** W-LD, **c** SLM-SD **d** SLM-TD, after electrochemically etched with 10% of oxalic acid **e** SLM-SD and **f** SLM-TD Fry’s etching

approximately 80 μm with a layer thickness of 18 μm . Along the selective direction of the laser melted, strip-like tissues were observed. The presence of bulk austenite can be seen in the region near the molten pool line (Fig. 3d).

The attack with Fry's reagent (5 g of CuCl_2 , 40 ml of HCl, 25 ml of ethanol and 30 ml of H_2O) in SLM-SD revealed evident signs of dendritic segregation, Fig. 3e. These heterogeneities were developed as a consequence of the complex and successive passes of the laser beam. Also, Fig. 3f shows large elongated grains growing parallel to the built direction, which can be seen around the limits of the track in SLM-TD. The differences in cooling rates at the melt pool zone are produced because of a high degree of convection heat transfer. Therefore, a finer and equiaxed microstructure was formed. Nevertheless, close to the melt pool edge, the cooling rate is lower. Therefore, elongated and larger grains were formed. Zhong et al. [31] and Trelewicz et al. [32] report similar results.

X-ray diffraction spectra (Fig. 4) shows the existence of different solid solutions and precipitates. These phases were similar for both the Wrought and SLM samples. Wrought 17–4 PH steels usually have a fully α' -martensitic (BCC) microstructure similar to that observed by Hsiao et al. [33]; however, the presence of austenite-stabilizing elements, such as Cu or Ni, can decrease the martensite start temperature (M_s). This gives rise to an incomplete martensite transformation, and consequently, it is relatively common to also find retained γ -austenite (FCC) in the microstructure similar to that described by Rafi et al. [34].

X-Ray diffraction for SLM also showed the BCC peaks, which can correspond to either ferrite or martensite. Alnajjar et al. [19] deduced that the as-built SLM 17–4 PH steel had a delta ferrite microstructure. This ferritic structure

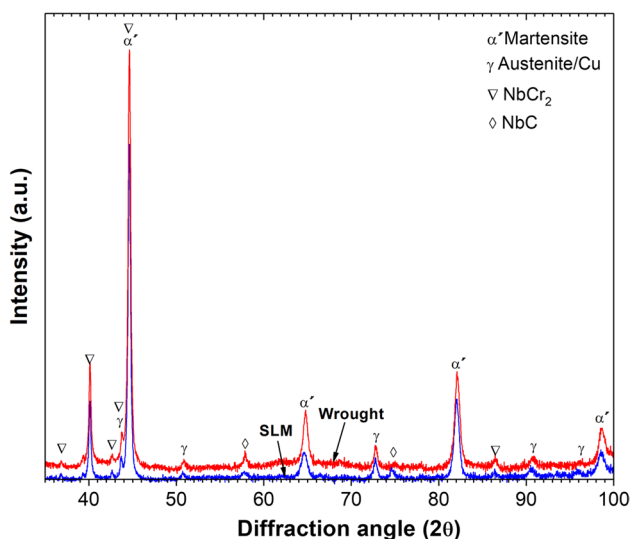


Fig.4 XRD spectra of testing samples

was justified by the high heating and cooling rates that do not allow austenite formation, so initial delta ferrite cannot be transformed. In this case, the presence of nitrogen as an austenite-stabilizing element allowed the formation of austenite which is partially transformed into martensite during rapid solidification cooling; so the martensite (α') was also the primary phase, and this fact was confirmed by the subsequent hardness measurements confirmed.

A slightly higher amount of γ -austenite (a high intensity γ (1 1 1) peak at 43.5°) than for W can also be identified. This is consistent with the lower ferrite percentage found in SLM (44.6% F) than in W (60.2% F). The reasons why SLM may have a higher amount of retained austenite are as follows: the use of nitrogen atmosphere during the SLM process, as the grain refinement observed in the SLM samples can lower the temperature M_s , also observed by Rafi et al. [34]; the grain boundaries where the atomic arrangement are irregular hinder the growth of martensite, in accordance with the literature [35]; and the dendritic segregation observed in SLM can lead to the enrichment of Ni, which can lead to the formation and stabilization of the austenite, as suggested by Caballero et al. [36]. The X-ray diffraction patterns also revealed the presence of precipitates. Furthermore, Nb-Cr intermetallic phases and complex Nb-Cr carbides were identified. The presence of copper precipitates cannot be discarded either, since the diffraction peaks coincide with those of the austenitic phase.

The SEM analysis of the microstructure of W and SLM revealed fine Nb-rich phases in both materials. In Fig. 5a, corresponding to W, light precipitates could be observed on the edges of the martensite plates. These very small precipitates are more visible in the sample in the polished state, Fig. 5b. Large inclusions dispersed in the matrix were observed for wrought samples, Fig. 5c. For SLM, the analysis of the microstructure within individual melt pools (Fig. 5d) also revealed fine precipitates, which were small, spherical-shaped particles and were especially visible along the dendrite boundaries. The small size of the precipitates makes it difficult to analyze them by EDS, but in both samples an increase in Nb and Cr contents were observed in these areas. These microstructural features are consistent with Cheruvathur et al. [37].

The EDX analysis indicated that the inclusion was MnS type and contained Fe, Cr, and O. The MnS inclusions content of SLM samples was much lower than for the W samples. This could be related to the insufficient time for nucleation due the high cooling rates that can be achieved during their fabrication [19]. An enhancement of corrosion resistance has been proven for inclusions of free stainless steels [19]. The typical Cu-rich precipitates were not observed in any of the analyzed samples, as their small size (between 15 and 30 nm) requires TEM microscopy for detection, which was used by Sarkar et al. [38] and Sanjeev et al. [39].

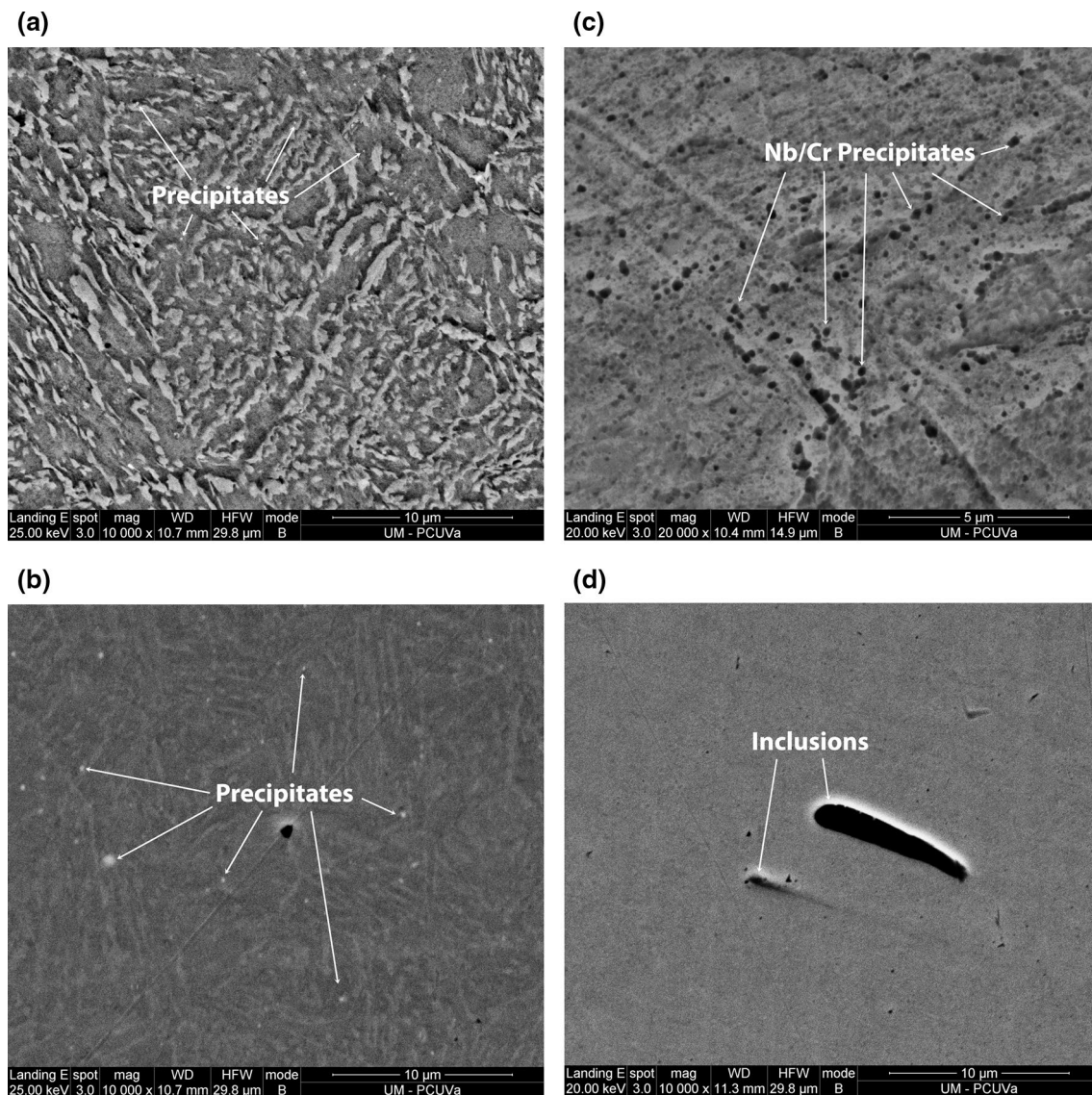


Fig. 5 SEM images showing the microstructure of a, b, c W and d SLM

3.2 Macro and Microhardness

Figure 6 displays the macro- and microhardness of SLM and W samples for the two analyzed sections. The macrohardness values are slightly higher than those of the microhardness. This indicates that the degree of porosity of the samples is low in both materials. Moreover, both tests showed the same tendency. The hardness results were similar for both the W and SLM samples, confirming the martensitic structure obtained from both fabrication methods.

The results of the macro- and microhardness tests showed that SLM-TD have a slightly lower hardness value than W-TD. However, Sarkar et al. [38], Shrestha et al. [8], and Sanjeev et al. [39] have all observed the opposite tendency, that the samples obtained by additive manufacturing are the

hardest. So, the high cooling rate associated to the SLM process produced the finer grain microstructure that explains this hardening, according to the Hall–Petch effect: the hardness would increase as the grain size decreases in accordance with the literature [40]. In addition, the higher density of dislocations adjacent to the grain boundaries of a finer grain structure also results in higher hardness values compared to the coarser grain structures of samples processed by plastic deformation, as has been said by Dieter [40].

In explaining the results obtained in this work, it must be considered that the samples were in different treatment conditions, i.e., the SLM samples were in as-built condition, while the W samples were in heat-treatment condition. It is well known that coherent Cu-rich precipitates are responsible for the increase of hardness in 17–4 PH. The Cu-rich precipitates

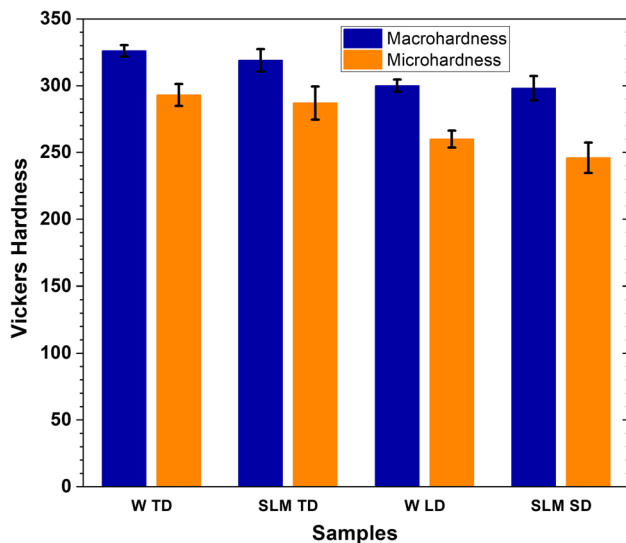


Fig. 6 Vickers hardness and microhardness of every as-fabricated samples

formed during aging are effective in preventing the movement of dislocations and provide a semi-coherent interface, which hardens the alloy, as seen in Sarkar et al. [38] and Zitelli et al. [41]. Therefore, in the as-produced state, the SLM material is typically softer than wrought and age hardened material; this was also observed by Guo and Kindt [42]. Additionally, another microstructural feature could explain the lower hardness of SLM samples, such as the amount of austenite phase. Yadollahi et al. [11] observed that the hardness of 17–4 PH SS samples is typically reduced with higher amounts of retained austenite phase; while this phase can be beneficial in increasing ductility and elongation. The lower magnetic response of SLM samples as compared to the W samples could indicate higher austenite content, which would result in lower hardening.

In both manufacturing methods, the samples in the normal direction were slightly harder than in the built direction for the SLM samples or in the longitudinal section for the W samples. The differences are more remarkable for the samples obtained by additive manufacturing. As Hu et al. [13] concluded, the microstructural heterogeneities derived from the additive manufacturing could explain these differences. The higher values of standard deviation observed in SLM-SD and SLM-TD, also noticed by Yusuf et al. [43], could also be a consequence of such heterogeneities (dendritic segregation, grain morphology, differences in cell grain size, etc.).

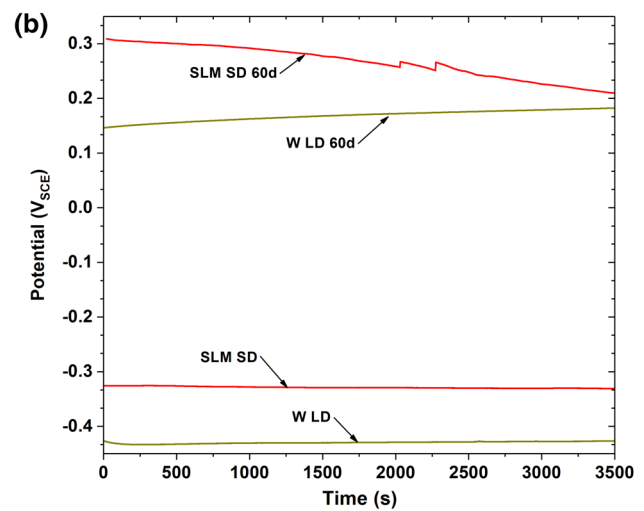
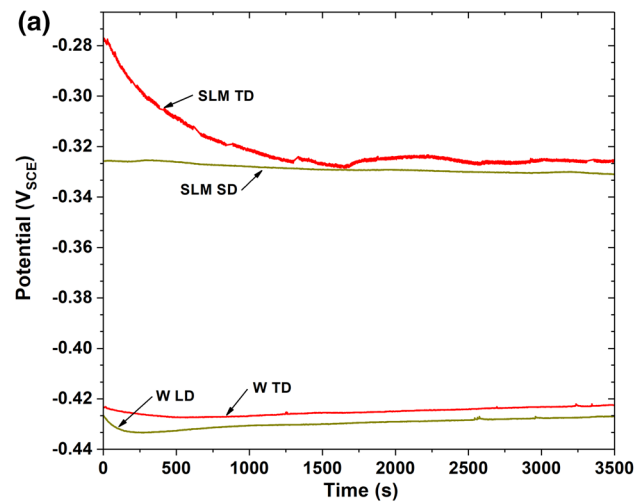


Fig. 7 OCP evolution of **a** as-fabricated samples and **b** SLM-SD and W-LD samples in acid solution with chlorides after 0 and 60 days of immersion

3.3 Corrosion Behavior

3.3.1 Open Circuit Potential

The evolution of OCP over time was used as an indicator to evaluate the thermodynamic tendency to corrosion of the SLM and W samples in a corrosive environment; the effect of the orientation of the samples was also analyzed to determine the isotropic or anisotropic corrosion behavior of the materials.

Figure 7a shows the plots of OCP vs. immersion time for all the samples. The OCPs for SLM-TD and SLM-SD are clearly more positive than for W-LD and W-TD. The nobler potential values indicate the formation of a more stable passive oxide layer on the surface of SLM samples, which implies a reduction in the thermodynamic tendency to corrosion and, therefore, an improvement in corrosion behavior.

The morphology of the plot of the OCP with the immersion time was clearly different as a function of the manufacturing technique used for processing the samples. The OCP for W-LD and W-TD shifted negatively during the initial period, before increasing steadily up to 1 h immersion. This suggests the dissolution of steel in the first period of the test and a continuous formation of a passive layer after 500 s of immersion time. On the contrary, the nearly plane curve observed in SLM-TD, after an initial dissolution, indicates that a dynamic equilibrium has been reached, which implicates the simultaneous dissolution and formation of the oxide layer. Furthermore, for SLM-SD, an unchanged potential during the immersion time was observed. Therefore, the passive oxide layer remains protective. At the end of the test, no important difference between SLM-SD and SLM-TD was found, which indicates an isotropic behavior for the samples processed by SLM; also, W-TD had a slightly higher potential than W-LD, although the differences were not very significant.

Finally, the samples were immersed in corrosive medium for 60 days and the variation in the OCP values with respect to the initial ones was analyzed. Figure 7b shows the shift to more positive values of OCPs as the samples were exposed to the solution, exhibiting a better corrosion resistance; this improvement was more intense for W-LD. Thus, the differences between the two processing techniques are attenuated.

3.3.2 Anodic Polarization Measurements

The results of the anodic polarization scans are presented in Fig. 8. They have been used to understand the anodic behavior of 17–4 PH SS in a solution containing chloride and can therefore cause localized attacks for different processing conditions, orientations and heat treatments. The potentiodynamic scans shown in Fig. 8a indicate that the curves for the four electrodes do exhibit a similar morphology; all the curves undergo local corrosion described by an important increase in the current density at breaking potential, where the pitting corrosion is started. However, there were differences between the samples depending on their processing method; while differences in the anodic polarization scans were also observed between SLM-SD and SLM-TD, but they were not as meaningful as the differences between W-LD and W-TD.

The cathode branch was moved to a higher potential for SLM samples. The anodic branch, which corresponds to the

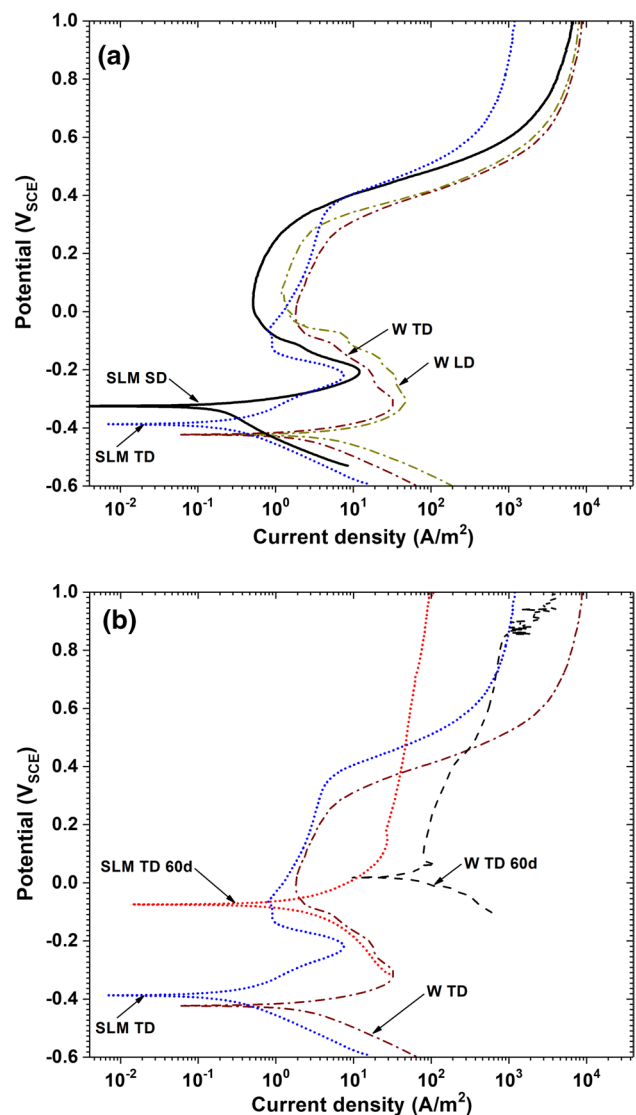


Fig. 8 Potentiodynamic polarization curves of **a** as-fabricated samples, **b** SLM-TD and W-TD samples in acid solution with chlorides after 0 and 60 days of immersion

dissolution of the metal and the generation of the passive layer, was also more stable and displayed nobler potentials for the SLM samples. The current density was smaller for SLM-TD and SLM-SD than for W-TD and W-LD; despite their heat treatment condition, the SLM-SD showed the highest breakdown potential and the widest passive potential range.

W-LD and W-TD showed similar anodic behavior; however, some differences between the two orientations of the SLM samples were observed. A lower passivity current could be easily identified for both SLM-SD and SLM-TD, although the latter had a slightly wider and more stable passive window. The microstructures presented in Fig. 2 are

significantly different and this could lead to some of these changes in electrochemical behavior.

The corrosion current density (i_{CORR}) and corrosion potential (E_{CORR}), obtained from the interpolation of the cathode and anode curves by Tafel analysis, the polarization resistance (R_p) and the breakdown potential (E_B) are all presented in Table 4. Comparatively, the highest E_{CORR} estimated for SLM-SD and SLM-TD is supported by the highest open circuit potential and suggests the material made by additive manufacturing is more resistant to dissolution. The i_{CORR} of W-TD and W-LC were found to be

clearly higher than those observed in SLM-SD and SLM-TD, so the polarization resistance values were almost an order of magnitude higher for the SLM samples than for the W samples. The inflection point for the fast increase in the current density with a minor change in potential was defined as the E_B . Compared to W-TD, the highest E_B recorded for the SLM-TD sample would indicate a higher stability of the oxide film. In no case were current fluctuations observed in the passive region, suggesting that a compact oxide film is formed.

Figure 8b shows the anodic behavior of the samples after 60 days of exposure to the aggressive solution. The immersion time had a similar effect for both SLW-TD and W-TD; thus, a significant increase in the corrosion potential and a clear improvement in the passive behavior (E_B increased and the passivity range was wider) were observed. However, a notable increment in the current densities was observed in both cases. The sample processed by additive manufacturing showed a lower current density and higher rupture potential than the sample obtained by the traditional method. This suggests the formation of a more compact and less defective passive film on SLM-TD, which could be related to its

Table 4 Electrochemical parameters estimated by Tafel method

Sample	E_{CORR} (V)	I_{CORR} (mA/cm ²)	R_p (Ω /cm ²)	E_B (mV)
W-LD	−423	1.44	30.34	253
W-TD	−423	0.74	64.50	260
W-TD -60d	18.9	8.50	2.29	855
SLM-SD	−325	0.024	557.5	256
SLM-TD	−388	0.021	687.6	342
TD-60d	−74	0.54	11.75	986

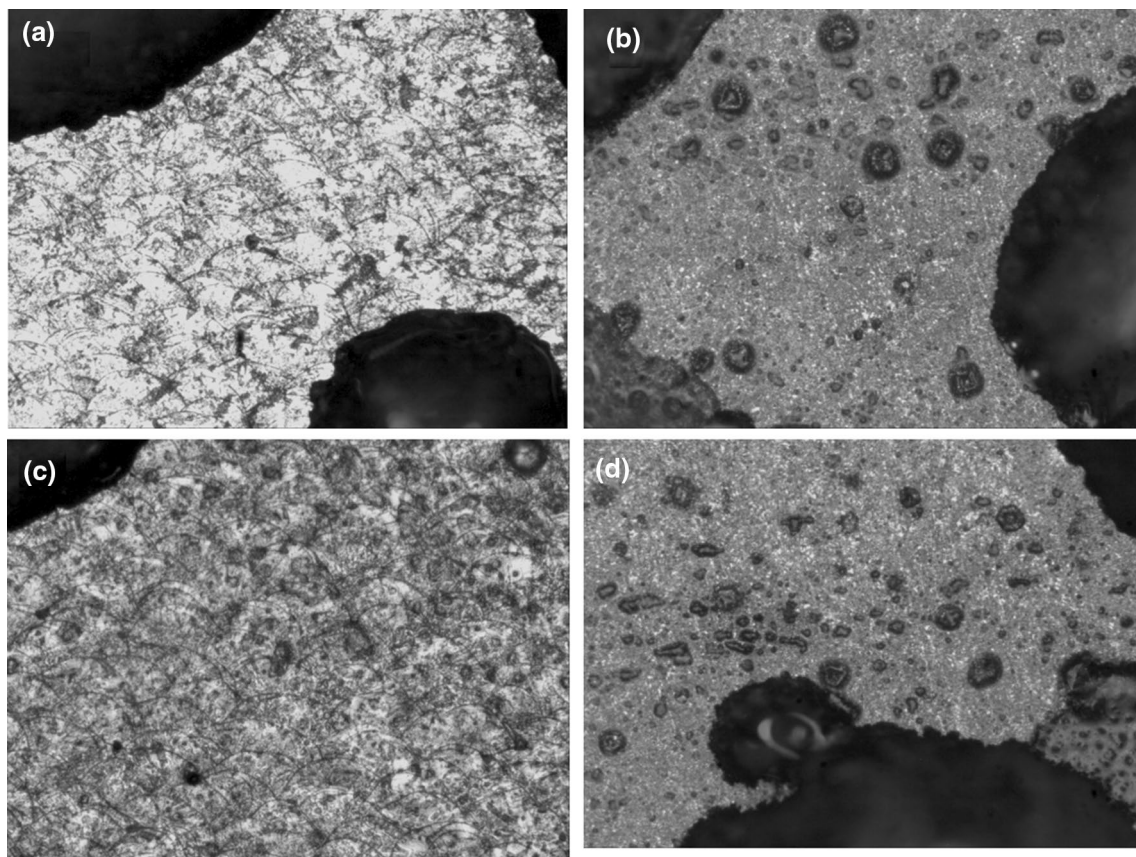


Fig. 9 Pitting produced during the potentiodynamic scans: **a** SLM-SD, **b** W-LD, **c** SLM-SD 60 days and **d** W-LD 60 days

Fig. 10 Nyquist **a** and Bode **b** and **c** plots of W-LD and SLM-SD samples in acid solution with chlorides after 0 days and 60 days of immersion. Results of the fitting to the equivalent electric circuit **d** are included

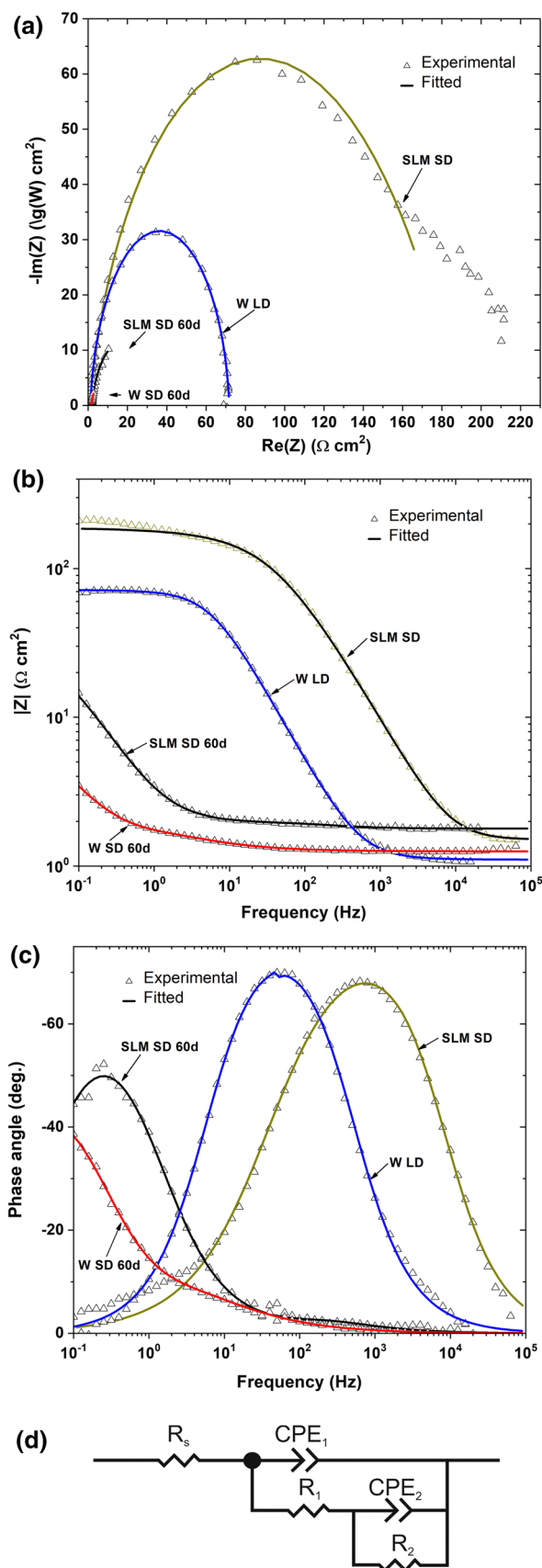
fine sub-grain microstructure, to a high amount of austenite phase and to a lower amount of non-metallic inclusions.

The electrode surfaces were examined under an optical microscope after an anodic polarization scan. Representative surfaces for each condition are presented in Fig. 9. In Fig. 9a, the W-LD sample shows significant pitting on what are probably MnS inclusions, as well as some additional pitting at the carbide-martensite interfaces. Both orientations of the SLM samples exhibit small pits, which are visible within the melt pools highlighted for the SLM-SD sample, Fig. 9b. Since these pits appeared to follow the general shape of the melt pools, they were attributed to compositional heterogeneities near the melt pool interfaces in this condition. After the exposure of the aggressive solution, the overall density of observable pitting was also considerably lower in the SLM samples, Fig. 9c, than that observed for the wrought material, Fig. 9d.

3.3.3 Electrochemical Impedance Spectroscopy measurements

The potentiostatic and potentiodynamic tests described above are the most commonly used to evaluate the corrosion resistance of stainless steels thermodynamically and kinetically, respectively. However, possible interference of the cathodic reaction at the electrode surface could compromise the accuracy of the results obtained with these methods, as mentioned in Wang et al. [44]. Therefore, electrochemical impedance spectroscopy has been used as a non-destructive technique to characterize the electrochemical interface between the electrodes and the electrolyte and could be used to provide more information about the physic-chemical processes taking place in 17–4 PH SS, i.e., the corrosion mechanisms that would occur while corroding in the acidic NaCl solution. Moreover, this technique, which has been successfully used in austenitic stainless steels produced by additive manufacturing, has scarcely been investigated for 17–4 PH SS.

As an example, the Bode and Nyquist diagrams for SLM-SD and W-LD at OCP are presented in Fig. 10; similar capacitive semicircles were observed in all cases, in that a uniform passive film had been formed on the surface of samples. The Nyquist curves, Fig. 10a, showed a depressed and unfinished semicircle in all cases. The stability of the oxide film can be analyzed by Nyquist plots. The larger diameter of semi-circle observed for SLM-SD represents a better stability of the film and a higher resistance to dissolution. It has also been observed in other more widely studied stainless



steels, such as 316 in different environments, as in the works of Lodhi et al. [45] and Al-Mamun [46] and also in 15–5 PH SS [20, 21].

The Bode diagram in Fig. 10b and c revealed a clear capacitive behavior, as the impedance modulus was almost one order of magnitude higher for SLM-SD. Since the impedance module value at the lowest frequency is associated with the barrier properties of the native oxide layer on the surface of the specimens, it indicates a higher corrosion resistance for the SLM samples as compared to the wrought specimens. Two-time constants, related to the capacitive behavior of the double layer and the oxide layer, can be identified in this phase angle change with frequency. In Bode's graph of the phase angle vs frequency, Fig. 10c, the phase angles in the mid-frequency region are close to -70° for both samples. This shows that the layer formed has a capacitive behavior. The maximum point of the offset angle is shifted into the lower frequency region for SLM-SD as compared to W-LD.

This enhanced passive film is in good agreement with the open circuit potential and anodic polarization tests, in which higher potentials and slightly lower passivity currents were observed for the SLM samples as compared to the wrought samples, respectively.

The effect of the immersion time in the aggressive solution for 17–4 PH SS is similar for both SLM and W samples. As can be observed from the Nyquist and Bode diagrams, Fig. 9, corresponding to samples immersed in aggressive solution for 60 days, the prolonged exposure to the solution resulted in a notable decrease in the radius of the semicircle of the impedance module and the phase angles. Despite this deterioration, the SLM-SD still showed a greater resistance than the W-LD.

An appropriate equivalent electronic circuit was selected in order to better understand the impedance spectra. After some trials with other typical circuits, Fig. 9d shows the proposed circuit. Figure 9 also collects the results of the fitting, while Table 5 shows the fitting parameters. To evaluate the quality of the fittings, the Chi-square values, χ^2 , were used. The variable χ^2 was to the order of 10^{-4} .

In the proposed circuit, the high frequency is related to a solution resistance (R_s); while the response at low and medium frequencies is related to the charge distribution

in the non-faradaic (double layer) and faradaic processes taking place at the interface of sample and solution.

The depression of the semicircle in the Nyquist diagram and the phase shift ($> -90^\circ$) lead us to postulate the presence of constant phase elements (CPE) instead of pure capacitors. The impedance of a CPE is defined as:

$$Z_{CPE} = \frac{1}{C(j\omega)^n}$$

where the CPE is an ideal capacitor for $n=1$; the CPE is an ideal resistor for $n=0$; and the CPE is a pure inductance for $n=-1$. The coefficient was $n < 1$, and is related to a non-homogeneous distribution of the load on the metal-electrolyte interface, specifying that C is not a real capacitance and the unit is $s^n \Omega^{-1} \text{cm}^{-2}$ rather than of F cm^{-2} .

The electric circuit model contains two-time constants, which are two layers in parallel. The first is the parallel combination of CPE_1 and R_1 in the layer impregnated with electrolyte. The electrolyte can penetrate through the pores of the passive layer and cause the metal to dissolve, generating a second time constant. The second relates to the parallel combination of R_2 and CPE_2 along the inner oxide film. This model has been successfully used to adjust the impedance spectra of stainless steels by Al-Mamun et al. [42]. So, the polarization resistance in the electrolyte, R_p (sum of R_1 and R_2), is stated in a low frequency limit ($f < 1$ Hz) and it signifies the resistance to electric charge transport through the film and across the oxide/electrolyte interface and could be associated to the corrosion resistance.

It can be seen that the R_s values are not influenced by the sample difference in the high frequency region since they were very low. This indicates the highly corrosive nature of the test solution. In addition, the values of R_1 and C_{1-n} , for all the samples, were clearly inferior to R_2 and C_{2-n} ; this confirmed the defective nature of the external layer in contact with the electrolyte. Despite this, the values of R_1 and C_{1-n} are clearly higher for SLM-SD as compared to W-LD. SLM-SD also has higher R_{IN} values and lower C_2 -C capacitance values than W-LD. Therefore, the better corrosion resistance of the film of SLM-SD is clear through the increase in R_p over W-DL (393.7 and 164.1 respectively) and further affirmed the enhanced corrosion resistance of the SLM 17–4PH SS.

Table 5 EIS equivalent circuit parameters of W-LD and SLM-SD samples before and after 60 days

Samples	R_s (Ωcm^2)	C_2 -C ($s^n \Omega^{-1} \text{cm}^{-2}$)	C_{2-n}	R_2 (Ωcm^2)	C_1 -C ($s^n \Omega^{-1} \text{cm}^{-2}$)	C_{1-n}	R_1 (Ωcm^2)	χ^2
W-LD	1.07	1.8 E-4	0.92	2.02	6.7 E-5	1.0	68.47	1.9 E-4
SLM-SD	1.51	1.5 E-5	0.98	1.48	1.6 E-4	0.60	184.9	10 E-4
W-LD-60	1.26	2.8 E-1	0.61	0.97	2.6 E-1	0.89	21.28	1.4 E-4
SLM-SD-60	1.80	2.1 E-2	0.76	0.23	7.3 E-2	0.86	29.3	8.6 E-4

For samples exposed to the acidic chloride solution, the decrease in R_p and the increase in CPE-C, observed for SLM-SD-60, demonstrated the negative impact of the exposure time on its corrosion resistance. A similar tendency was detected for the W-LD-60 sample, which further confirms the deleterious effects of chloride ions. This behavior has been observed on 316L SS by Al Saadi et al. [47] and has been related to the adverse interaction of Cl^- ions with the oxide film. The Cl^- species can accelerate localized anodic reactions, because of its strong depolarization tendency and the formation of complexes soluble in water. Jones et al. [48] found that this effect is more intense the longer the time of interaction with the stainless steel.

4 Discussion

The objective of this work is the study of the electrochemical behavior of 17–4 PH steel processed by SLM in chloride containing acidic medium. Chloride ions are known to adsorb and penetrate the oxide film of stainless steels and, when the concentration exceeds a critical value, the passive film is destroyed in the favored sites, such as the defective areas, as shown by Suryawanshi et al. [29] on some selective laser melted alloys. Thus, Hao et al. [49] developed a model based on point defects that explains the destruction of passivity on the surface of passive metals by assuming that cationic vacancies migrate from the oxide film-electrolyte interface to the metal/oxide film interface. Oxide film rupture occurs as a result of stresses in the oxide film caused by vacancies in the metal/oxide film interface. In addition, the migration of chloride ions, aided by oxygen vacancies, causes the localized dissolution of this passive film. Manufacturing defects such as pores and cracks at the bottom or at the interface of the molten pool line had a negative effect on corrosion resistance. Despite the above, SLM-SD has higher resistance values and lower capacitance values than W-LD. These results suggest the formation of a more compact and less defective oxide film on the SLM 17–4 PH SS sample thanks to the small amount of manufacturing defects in SLM samples.

The calculated electrochemical impedance results suggest that the SLM technique has a better corrosion resistance for 17–4 PH SS than the conventional processed method in an acid-chloride environment, consistent with the open circuit and anodic polarization results. This corrosion behavior should be related to the microstructure features observed for these samples and with the chemical composition of the material. The high content of Cr and Cu in the powder could improve the corrosion resistance of passive film.

Furthermore, to analyze these results, it should be taken into account that the processed 17–4 PH SS SLM was an in-built condition; while the wrought SS was heat treated,

so a direct comparison between the two materials is difficult. The heat treatment could explain the slightly higher macro and microhardness observed for W samples. After aging, the precipitation of Cu-rich nanoparticles could originate an important hardening.

The influence of these Cu nanoprecipitates on corrosion resistance is controversial. Heat-treated steel samples are normally more resistant to corrosion, so SS steels fabricated by SLM have a slightly lower corrosion resistance compared to heat-treated wrought SS; as indicated in the study by Stoudt et al. [22]. These suggested the need for a homogenizing heat treatment, whereby additively produced SS17–4 could be more resistant to pitting than wrought 17–4 PH SS in a chloride environment.

However, a recent study showed that the corrosion resistance of SLM 15–5 PH steel after heat treatment was significantly reduced [21]. In good correlation with this, the results obtained in this work show that the non-heat treated SLM samples have a higher corrosion resistance than the heat treated W sample. In this work, there is a significant shift in the anodic curves towards higher potentials. Lower current densities and higher polarization resistance values were observed in the samples processed by additive manufacturing without homogenization heat treatment.

The best anodic performance of the 17–4 SS SLM as compared to the 17–4 SS W has also been observed in other SS, such as 316L, by Laleh et al. [50] and Stull et al. [51]. This was explained as a function of the passive oxide film's stability and pitting resistance parameters. Annamalai et al. [52] found that the tendency to form a passive film depends on a number of factors, including the surface chemistry, grain structure and size, the degree of porosity, alloy element segregation, the inclusions, the precipitation of carbides and intermetallic phases, and the composition of the electrolyte, etc.

Additive manufacturing 17–4 PH SS are usually metallurgically inhomogeneous and have a high degree of porosity compared to wrought base metal. These are the two most important factors that deteriorate the corrosion resistance of the SLM-fabricated SS materials compared to conventionally manufactured samples, independently of the electrolyte environment. Thus, Annamalai et al. [52] and Panda [53] observed a negative response of ferritic and austenitic SS. Schaller et al. [17] established that zones with large pores ($d \geq 50 \mu\text{m}$) showed active dissolution versus the passive behavior shown by zones with smaller pores ($d \leq 10 \mu\text{m}$). In this work, the SLM samples appear to be fully densified; therefore, there is no evidence of large pores in the microstructural analysis at high magnifications.

Lodhi et al. [44] demonstrated that the fine grain structure obtained from the additive manufacturing process is associated with a higher corrosion resistance on SS. The structure of columnar grains and colonies forming a cellular

substructure of microns and submicrons is known thanks to Al-Mamun et al. [45] and Reynier et al. [54]. This facilitates the formation of a compact passive layer on SLM SS when the material is exposed to such passive media as NaCl solutions. The main mechanism for improving the corrosion resistance associated with grain refinement is related to the increased adhesion of the films on the SS as a consequence of a grain boundary density increase.

Furthermore, it is commonly accepted in the literature, as has been proven by Ryan et al. [55] and Muto et al. [56], that MnS inclusions are crucial for the initiation of pitting in chloride environments by generating Cr-depleted zones around MnS particles. The additive manufacturing process leads to rapid solidification, which diminishes or completely excludes the nucleation of MnS inclusions. According to Chao et al. [57], the higher content of such inclusions, observed in W samples, may also contribute to its poorer anodic behavior. Finally, the type of carbides and their morphology also influence corrosion behavior. Chromium-rich carbides can cause different forms of localized corrosion that will degrade the passive layer; while the higher niobium content of these carbides will leave the chromium available to form more resistant passive layers, as Stoudt et al. [22] also proved for additive manufacturing 17–4 PH. The small niobium-rich precipitates observed in the microstructure of the SLM samples would lead to an overall enhancement in the stability of the passive film.

Finally, the higher amount of nitrogen and the presence of an austenite phase at the bottom of the molten pool/martensite lath of SLM 17–4 PH SS could significantly improve the corrosion resistance of the stainless steel. Wang et al. proved that austenite formed on SLM 15–5 PH SS was rich in nickel and nitrogen, and this enrichment at the bottom of the passivation film affects the crystallinity of the passivation film and the chemical content of the passivation film, improving its pitting corrosion resistance [20]. This retained austenite in the as-built AM material could be transformed into martensite by heat treatment with a considerable increase in hardness [58]. In addition, nitrogen can improve the corrosion resistance of 17–4 PH stainless steels produced by additive manufacturing, as reported by Stoudt et al. [20]. The homogeneous distribution of nitrogen in the retained austenite and the precipitation of NbCN could produce a more stable passive film. Based on these results, the nitrogen content in SLM 17-PH ($0.0829 \pm 0.0007\%$ w) seems to have a beneficial influence on localized corrosion resistance.

5 Conclusions

This study has revealed that SLM additive manufacturing can be successfully used to produce metal components in 17–4 PH SS with comparable and sometimes superior properties to those of its commercial counterparts.

17–4 PH SS can be processed in SLM processes to almost full relative density. The microstructure of SLM 17–4 PH SS is, as is to be expected, dominated by the high cooling rates, with evident signs of dendritic segregation. The anisotropic and complex structure formed during solidification consists of a mixture of a finer microstructure and elongated and coarser grains with an important amount of austenite formed at the bottom of the molten pools.

The macro/micro hardness of steels produced by SLM is slightly lower than that of conventionally produced counterpart steels. This is justified by the higher amount of austenite retained and the lower amount of precipitates of as-built SLM specimens compared to heat-treated wrought samples.

The electrochemical behavior of wrought 17–4 PH SS and SLM was studied in an acid solution with chlorides. An open circuit potential test, potentiodynamic polarization measurement and spectroscopy impedance analysis, recorded as the fabricated condition and after 60 days of immersion of the samples, revealed that the SLM samples, in addition to having a more noble corrosion potential, also showed improvements in passive behavior, with lower current densities in the anodic branch of the polarization curve, all without obvious signs of localized corrosion and higher electron transfer resistance. Corrosion testing confirmed that the SLM samples showed the best corrosion performance, even at long immersion times, independently of the build orientation.

The samples processed by SLM showed a greater resistance to corrosion than those processed by the traditional method, despite not having heat treatment. The absence of important manufacturing defects and the fine martensitic microstructure with significant amounts of nitrogen in austenite and a small content of non-metallic inclusions as a result of the fast cooling and the high speed of solidification associated with the SLM process could contribute to this behavior.

Funding Open Access funding provided thanks to the CRUE-CSIC agreement with Springer Nature. This work was supported by Ministry of Science, Innovation and Universities (Plan Nacional: RTI2018-097990-B-I00) and the Junta de Castilla y Leon (VA275P18) and (VA044G19).

Declaration

Conflict of interest The authors declare no conflict of interest.

Open Access This article is licensed under a Creative Commons Attribution 4.0 International License, which permits use, sharing, adaptation, distribution and reproduction in any medium or format, as long as you give appropriate credit to the original author(s) and the source, provide a link to the Creative Commons licence, and indicate if changes were made. The images or other third party material in this article are included in the article's Creative Commons licence, unless indicated otherwise in a credit line to the material. If material is not included in

the article's Creative Commons licence and your intended use is not permitted by statutory regulation or exceeds the permitted use, you will need to obtain permission directly from the copyright holder. To view a copy of this licence, visit <http://creativecommons.org/licenses/by/4.0/>.

References

- C.Y. Yap, C.K. Chua, Z.L. Dong, Z.H. Liu, D.Q. Zhang, L.E. Loh, S.L. Sing, *Appl. Phys. Rev.* **2**, 041101 (2015)
- L.E. Murr, S.M. Gaytan, D.A. Ramirez, E. Martinez, J. Hernandez, K.N. Amato, P.W. Shindo, F.R. Medina, R.B. Wicker, *J. Mater. Sci. Technol.* **28**, 1 (2012)
- T. Maconachie, M. Leary, B. Lozanovski, X. Zhang, M. Qian, O. Faruque, M. Brandt, *Mater. Design* **183**, 108137 (2019)
- J. Hunt, F. Derguti, I. Todd, *Ironmak. Steelmak.* **41**, 254 (2014)
- Z.C. Fang, Z.L. Wu, C.G. Huang, C.W. Wu, *Opt. Laser Technol.* **129**, 106283 (2020)
- A. Sola, A. Nouri, *J. Adv. Manuf. Process.* **1**, 21 (2019)
- D. Wang, C.T. Chi, W.Q. Wang, Y.L. Li, M.S. Wang, X.G. Chen, Z.H. Chen, X.P. Cheng, Y.J. Xie, *J. Mater. Sci. Technol.* **35**, 1315 (2019)
- R. Shrestha, N. Shamsaei, M. Seifi, N. Phan, *Addit. Manuf.* **29**, 100807 (2019)
- R. Rashid, S.H. Masood, D. Ruan, S. Palanisamy, R.A.R. Rashid, M. Brandt, *J. Mater. Process. Tech.* **249**, 502 (2017)
- A. Kudzal, B. McWilliams, C. Hofmeister, F. Kellogg, J. Yu, J. Taggart-Scarff, J. Liang, *Mater. Design* **133**, 205 (2017)
- A. Yadollahi, N. Shamsaei, S.M. Thompson, A. Elwany, L. Bian, *Int. J. Fatigue* **94**, 218 (2017)
- X.D. Nong, X.L. Zhou, *Mater. Charact.* **174**, 111012 (2021)
- Z. Hu, H. Zhu, H. Zhang, X. Zeng, *Opt. Laser Technol.* **87**, 17 (2017)
- M. Mahmoudi, A. Elwany, A. Yadollahi, S.M. Thompson, L. Bian, N. Shamsaei, *Rapid Prototyp. J.* **23**, 280 (2017)
- Y. Wang, N. Wang, C. Yan, T. Zhang, L. Chen, J. Gu, *Mater. Test.* **62**, 5 (2020)
- H. Irrinki, T. Harper, S. Badwe, J. Stitzel, O. Gulsoy, G. Gupta, S.V. Atre, *Prog. Addit. Manuf.* **3**, 39 (2018)
- R.F. Schaller, J.M. Taylor, J. Rodelas, E.J. Schindelholz, *Corrosion* **73**, 796 (2017)
- G. Ko, W. Kim, K. Kwon, T.-K. Lee, *Metals* **11**, 516 (2021)
- M. Alnajjar, F. Christien, V. Barnier, C. Bosch, K. Wolski, A.D. Fortes, M. Telling, *Corros. Sci.* **168**, 108585 (2020)
- L. Wang, C. Dong, D. Kong, C. Man, J. Liang, C. Wang, K. Xiao, X. Li, *Steel Res. Int.* **91**, 1900447 (2020)
- L. Wang, C. Dong, C. Man, D. Kong, K. Xiaoa, X. Lia, *Corros. Sci.* **166**, 108427 (2020)
- M.R. Stoudt, R.E. Ricker, E.A. Lass, L.E. Levine, *JOM* **69**, 506 (2017)
- S.B. Mujib, S. Mukherjee, Z. Ren, G. Singh, *R. Soc. Open Sci.* **7**, 200214 (2021)
- P. Leo, S. D'Ostuni, P. Perulli, M.A.C. Sastre, A.I. Fernández-Abia, J. Barreiro, *Procedia Manuf.* **41**, 66 (2019)
- ISO/ASTM 52900:2015, Additive manufacturing-General principles-Terminology (International Organization for Standardization, Geneva, 2015)
- ASTM G-5-87, Standard reference test method for making potentiostatic and potentiodynamic anodic polarization measurements (ASTM International, West Conshohocken, 1993)
- J. Suryawanshi, T. Baskaran, O. Prakash, S.B. Arya, U. Ramamurty, *Materialia* **3**, 153 (2018)
- N.T. Aboulkhair, N.M. Everitt, I. Ashcroft, C. Tuck, *Addit. Manuf.* **1-4**, 77 (2014)
- J. Suryawanshi, K.G. Prashanth, U. Ramamurty, *Mater. Sci. Eng. A* **696**, 113 (2017)
- Y. Zhang, D. Zhan, X. Qi, Z. Jiang, *J. Mater. Sci. Technol.* **35**, 1240 (2019)
- Y. Zhong, L. Liu, S. Wikman, D. Cui, Z. Shen, *J. Nucl. Mater.* **470**, 170 (2016)
- J.R. Trelewicz, G.P. Halada, O.K. Donaldson, G. Manogharan, *JOM* **68**, 850 (2016)
- C.N. Hsiao, C.S. Chiou, J.R. Yang, *Mater. Chem. Phys.* **74**, 134 (2002)
- H.K. Rafi, D. Pal, N. Patil, T.L. Starr, B.E. Stucker, *J. Mater. Eng. Perform.* **23**, 4421 (2014)
- W.D. Callister, *Material Science and Engineering: An Introduction*, 5th edn. (Wiley and Sons, Hoboken, 1994), pp. 45–58
- A. Caballero, J. Ding, S. Ganguly, S. Williams, *J. Mater. Process. Tech.* **268**, 54 (2019)
- S. Cheruvathur, E.A. Lass, C.E. Campbell, *JOM* **68**, 930 (2016)
- S. Sarkar, S. Mukherjee, C.S. Kumar, A.K. Nath, *J. Manuf. Process.* **50**, 279 (2020)
- K.C. Sanjeev, P.D. Nezhadfar, C. Phillips, M.S. Kennedy, N. Shamsaei, R.L. Jackson, *Wear* **440-441**, 203100 (2019)
- G.D. Dieter, *Mechanical Metallurgy*, 3rd edn. (McGraw-hill, New York, 1986), pp. 34–45
- C. Zitelli, P. Folgarait, A. Di Schino, *Metals* **9**, 731 (2019)
- Z. Guo, J.T. Kindt, *Langmuir* **34**, 12947 (2018)
- S.M. Yusuf, N. Gao, *Mater. Sci. Technol.* **33**, 1269 (2017)
- X. Wang, M. Nie, C.T. Wang, S.C. Wang, N. Gao, *Mater. Design* **83**, 193 (2015)
- M.J.K. Lodhi, K.M. Deen, M.C. Greenlee-Wacker, W. Haider, *Addit. Manuf.* **27**, 8 (2019)
- N.S. Al-Mamun, K.M. Deen, W. Haider, E. Asselin, I. Shabib, *Addit. Manuf.* **34**, 101237 (2020)
- S.A. Saadi, Y. Yi, P. Cho, C. Jang, P. Beeley, *Corros. Sci.* **111**, 720 (2016)
- R.L. Jones, J. Stewart, *J. Non.-Cryst. Solids* **356**, 2433 (2010)
- S. Hao, P. Wu, J. Zou, T. Grosdidier, C. Dong, *Appl. Surf. Sci.* **253**, 5349 (2007)
- M. Laleh, A.E. Hughes, S. Yang, J. Li, W. Xu, I. Gibson, M.Y. Tan, *Corros. Sci.* **165**, 108394 (2020)
- J.A. Stull, M.A. Hill, T.J. Lienert, J. Tokash, K.R. Bohn, D.E. Hooks, *JOM* **70**, 2677 (2018)
- A. Raja Annamalai, A. Upadhyaya, D.K. Agrawal, *Can. Metall. Quart.* **54**, 142 (2015)
- S.S. Panda, V. Singh, A. Upadhyaya, D. Agrawal, *Scripta Mater.* **54**, 2179 (2006)
- I. Reynier, I. Revilla, B. Woutersa, F. Andreattab, A. Lanzuttib, L. Fedrizzib, I. De Graevea, *Corros. Sci.* **167**, 108480 (2020)
- M.P. Ryan, D.E. Williams, R.J. Chater, B.M. Hutton, D.S. McPhail, *Nature* **415**, 770 (2002)
- I. Muto, Y. Izumiyama, N. Hara, *J. Electrochem. Soc.* **154**, C439 (2007)
- Q. Chao, V. Cruz, S. Thomas, N. Birbilis, P. Collins, A. Taylor, P.D. Hodgson, *Scripta Mater.* **141**, 94 (2017)
- J.-R. Lee, M.-S. Lee, H. Chae, S.Y. Lee, T. Na, W.-S. Kim, T.-S. Jun, *Mater. Charact.* **167**, 110468 (2020)

Publisher's Note Springer Nature remains neutral with regard to jurisdictional claims in published maps and institutional affiliations.